Observing geomagnetic induction in magnetic satellite measurements and associated implications for mantle conductivity

Steven Constable and Catherine Constable

Institute of Geophysics and Planetary Physics, Scripps Institution of Oceanography, La Jolla, California 92093, USA (sconstable@ucsd.edu; cconstable@ucsd.edu)

[1] Currents induced in Earth by temporal variations in the external magnetic field have long been used to probe mantle electrical conductivity, but almost exclusively from sparsely distributed land observatories. Satellite-borne magnetometers, such as flown on Magsat, Ørsted, and Champ, offer the prospect of improved spatial coverage. The approach we have taken is to isolate induction by harmonic Dst ("disturbance storm time") excitation of the magnetospheric ring current in satellite magnetic measurements: this is done by removing the magnetic contributions of the main (core) magnetic field, the crustal magnetic field, and ionospheric fields (cause of the daily variation) using *Sabaka et al.*'s [2000, 2002] CMP3 comprehensive model. The Dst signal is then clearly evident in the midlatitude satellite passes lower than 50 degrees geomagnetic latitude. At higher latitudes, auroral and field aligned currents contaminate the data. We fit the internal and external components of the Dst signal for each equatorial pass, exploiting the fact that the geometry for the internal and external components is different for the azimuthal and radial vector components. The resulting timeseries of internal and external field variations shows that the Dst signals for the dawn passes are half those of the dusk passes. The sum of equatorial external and internal components of the field averaged over dawn and dusk passes provides an excellent estimate for the Dst index, and may in fact be superior when used as a proxy for the purposes of removing induced and magnetospheric fields from satellite magnetic data. We call this estimate satellite Dst. Cross spectral analysis of the internal and external timeseries shows both greater power and higher coherence in the dusk data. We processed the transfer function between internal and external dusk timeseries to provide globally-averaged, frequency dependent impedances that agree well with independently derived estimates. We estimate Earth's radial electrical conductivity structure from these impedances using standard regularized inversion techniques. A near-surface conductor is required, of thickness less than 10 km with a conductivity-thickness product almost exactly that of an average Earth ocean. Inversions suggest that an increase in conductivity at 440 km depth, predicted by recent laboratory measurements on high pressure phases of olivine, is not favored by the data, although, as in previous studies, the 670 km discontinuity between the upper and lower mantle is associated with a two orders of magnitude jump in conductivity. A new feature in our inversions is a further increase in lower mantle conductivity at a depth of 1300 km. A global map of the internal (induced) component of the magnetic field provides a qualitative estimate of three-dimensional (3-D) variations in Earth electrical conductivity, demonstrating graphically that the satellite data are responsive to lateral variations in electrical conductivity caused by the continents and oceans.

1. Introduction

[2] *Schuster* [1889] was first to note inductive effects associated with the daily variations of Earth's magnetic field. Since that time an industry has developed whereby currents induced in Earth by temporal variations in the external magnetic field have been used to probe mantle electrical conductivity [e.g., *Lahiri and Price*, 1939; *Banks*, 1969; *Schultz and Larsen*, 1987, 1990; *Constable*, 1993; *Olsen*, 1999a], but generally from sparsely distributed land observatories. Satellite-borne magnetometers, such as flown on Magsat, Ørsted, and Champ, offer the prospect of improved spatial coverage. However, the task of separating the temporal and spatial signals, mixed together as the satellite passes over regions of variable electrical conductivity while the external magnetic field varies in intensity and direction, is by no means trivial, and only a few authors have tackled this problem [e.g., *Didwall*, 1984; *Oraevsky et al.*, 1993; *Olsen*, 1999b]. Their efforts are thoroughly reviewed by *Olsen* [1999b], who noted that the shorter time series of satellite data tended to produce noisier results than ground data. In his new analysis of Magsat data, *Olsen* [1999b] found higher resistivity in oceanic than continental areas, but because of a lack of frequency dependence in the results he attributes at least part of this difference to causes other than mantle conductivity.

[3] In this paper we derive estimates of conductivity from frequency dependent impedance response functions generated from the ratio of internal to external parts of the geomagnetic field. The external source field we consider is that generated by Dst ("ring current") variations, over periods ranging from about 7 hours to 100 days. We use vector field data from Magsat and *Sabaka et al.*'s [2000] comprehensive magnetic field model to remove non-inductive components from the magnetic field data (i.e., crustal and main field signals) and ionospheric contributions (the daily variation). We generate complete time series of the inductive component (instead of selecting only energetic storm-time events), use modern, robust multitaper time series analysis, modern one-dimensional (1-D) regularized inversion studies, and generate qualitative global images of geomagnetic induction in Earth.

[4] The ultimate goal of this study is to image one-dimensional and three-dimensional electrical conductivity structure of Earth's mantle. One dimensional (1-D) structure is influenced most by pressure dependent phase changes, and probably represents the dominant conductivity signal within the mantle and core. Three dimensional (3-D) structure can provide information about lateral variations in temperature and trace volatiles in the mantle. In the crust, 3-D structure dominates the conductivity signal, reflecting the large lateral changes found in the temperature, porosity, and water content of crustal rocks, as well as the ocean/continent signal.

2. Dst and the Ring Current

[5] *Banks* [1969] showed that variations in Earth's magnetic field at periods shorter than one year are dominated by a simple P_1^0 spherical harmonic geometry. Later work confirms this, and determines the cause to be the excitation of the equatorial ring current, a westward propagating current between 2 and 9 Earth radii that is populated with charge carriers, mainly oxygen ions from the upper atmosphere, during magnetic storms driven by the solar wind (see the review by *Daglis et al.* [1999]). During quiescent times the ring current is populated mainly by protons. Excitation of the ring current serves to oppose Earth's main field at the equator, and so produces

a magnetic field aligned with main field at the poles (vertically down at the north pole).

[6] The strength of the ring current is characterized by the "Dst" (disturbance storm time) index, an index of magnetic activity derived from a network of low to midlatitude geomagnetic observatories that measures the intensity of the globally symmetrical part of the equatorial ring current. An early method for derivation of the Dst index is described in *Sugiura* [1964], the current method is updated in IAGA Bulletin No. 40, a report by Masahisa Sugiura which presents the values of the equatorial Dst index for 1957–1986. This can be found on the Web at http://swdcdb.kugi.kyoto-u.ac.jp/dst2/onDstindex.html. Honolulu, Hermanus, San Juan and Kakioka are the current contributing observatories. During the Magsat mission, Alibag provided supplemental longitudinal coverage.

[7] The actual morphology of the ring current fields is asymmetric about the day/night hemispheres [*Chapman and Bartels*, 1940], and strictly speaking one should preserve a distinction between Dst, the index, and the actual ring current fields, but we relax this distinction here for the sake of readability.

3. Isolating Dst From Satellite Observations

[8] Magsat flew from November 1979 to May 1980, and collected both vector and scalar magnetic field data in a sun-synchronous orbit. That is, the satellite passed from local solar dawn (06:00) to local solar dusk (18:00) during every orbit. Magsat's altitude ranged from 325–550 km. Vector fluxgate magnetometer data (approximate accuracy 6 nT) decimated to 0.1 Hz were used (M. Purucker, personal communication), and we rejected all measurements with attitude flag ≥7000. We used the Comprehensive Model of the Near-Earth Magnetic Field: Phase 3 [*Sabaka et al.*, 2000]. This model, designated CMP3, includes estimates of the following: The main (core) field, and its secular variation, the crustal (lithospheric) field due to remanent and induced magnetization, ionospheric currents (daily and storm-time variations), field aligned and meridional currents, and seasonal variations, equatorial

electrojet, magnetospheric ring current, and coupling and induction of the above. (A later version of the Comprehensive Model, designated CM3 [*Sabaka et al.*, 2002], was made available during the course of this work. We tested this version of the model and concluded that CMP3 did a slightly better job of fitting the Magsat data set than did CM3, and so kept our original analysis.)

[9] Parameters supplied to CMP3 for every data point are position in geomagnetic coordinates, magnetic universal time [*Sabaka et al.*, 2000], and insolation represented by the 10.7 cm radio flux. The ring current and storm-time variations are modeled via a dependence on the Dst index. We turned off this part of the model by setting Dst = 0 and use the residuals after predicting the vector Magsat data with CMP3 as our initial model. We designate these the "CMP3-Dst" residuals. (A 25 nT static component of the ring current is still supplied by CMP3.) Figure 1 presents a sample of these residuals for the total field (i.e., the total field residuals, not the magnitude of the vector residuals) as a function of magnetic colatitude. It is apparent that within 50° of the magnetic equator, the field varies smoothly with a P_1^0 geometry having a maximum near the equator. At higher latitudes, centered around colatitudes of 15° and 165°, incomplete removal of the auroral electrojets is apparent. Accordingly, we take only data within 50° of the geomagnetic equator for this study.

4. Fitting P_1^0 to Dst

[10] Dst has a predominantly P_1^0 structure in midlatitude regions in geomagnetic coordinates. We assume this to be a valid approximation between ±50° geomagnetic latitude, and that the CMP3-Dst residual can be used to provide an estimate of the internal $i_1^0(t)$ and external coefficients $e_1^0(t)$ at the average time, t, of each satellite pass. We convert between a geographic and geomagnetic coordinate system assuming a geomagnetic north pole located at a colatitude of 11.2° and a longitude of 289.3° [*Langel and Hinze*, 1998, p. 24].

[11] We write the observed field as the gradient of a scalar potential expressed as a spherical harmonic expansion of associated Legendre polynomials P_l^m,
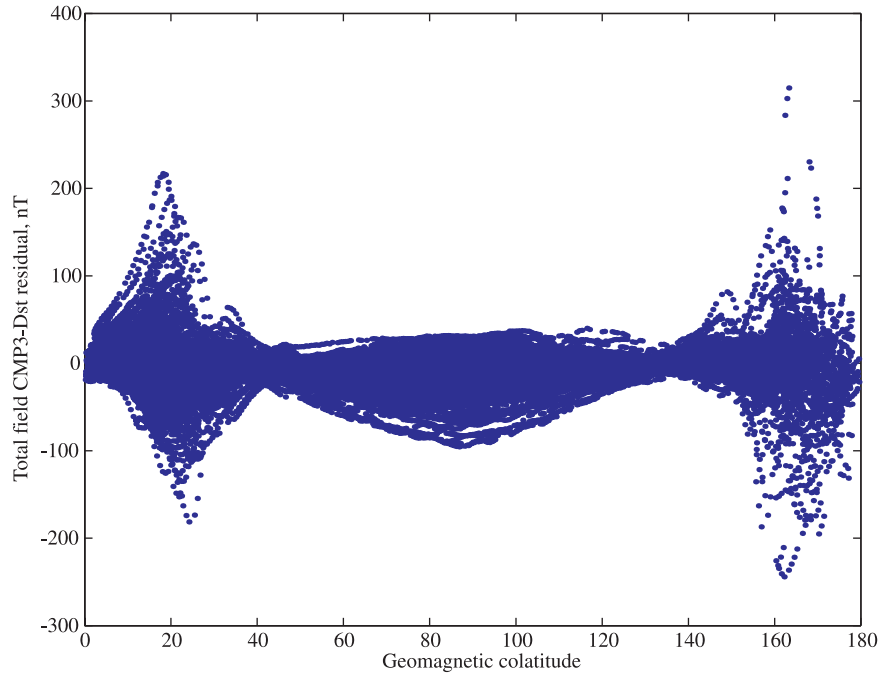
Figure 1. A sample of CMP3-Dst residuals (the first 100,000 data points) for the total magnetic field plotted as function of geomagnetic colatitude, θ_d. We use only observations in colatitude range $40° < \theta_d < 140°$ for our modeling to avoid magnetic fields associated with field-aligned currents, here evident as rapidly varying fields peaking within 20° of the poles.

with Schmidt quasi-normalized spherical harmonic coefficients representing the internal $i_l^m(t)$ and external $e_l^m(t)$ magnetic fields:

$$\Phi(r,\theta,\phi) = a_o \sum_{l=1}^{\infty} \sum_{m=-l}^{l} \left\{ i_l^m(t)\left(\frac{a_o}{r}\right)^{l+1} + e_l^m(t)\left(\frac{r}{a_o}\right)^l \right\} P_l^m(\cos\theta)e^{im\phi}.$$

Keeping only the P_1^0 contribution and with r, θ, ϕ in geomagnetic coordinates

$$\Phi_1^0(r,\theta) = a_o \left\{ i_1^0(t)\left(\frac{a_o}{r}\right)^2 + e_1^0(t)\left(\frac{r}{a_o}\right) \right\} P_1^0(\cos\theta)$$

and so the magnetic induction **B** is derived from the negative of the gradient in the usual manner

$$\mathbf{B}(r,\theta,\phi) = -\nabla\Phi_1^0(r,\theta,\phi)$$

or, expressed as components B_r, B_θ, B_ϕ of a spherical coordinate system:

$$B_r = \left[-e_1^0 + 2i_1^0\left(\frac{a}{r}\right)^3\right]\cos(\theta)$$

$$B_\theta = \left[e_1^0 + i_1^0\left(\frac{a}{r}\right)^3\right]\sin(\theta)$$

$$B_\phi = 0.$$

The above, neglecting the azimuthal (ϕ) component (which should be zero), may be expressed in matrix form as:

$$\begin{bmatrix} -\cos(\theta) & 2\left(\frac{a}{r}\right)^3\cos(\theta) \\ \sin(\theta) & \left(\frac{a}{r}\right)^3\sin(\theta) \end{bmatrix} \begin{bmatrix} e_1^0 \\ i_1^0 \end{bmatrix} = \begin{bmatrix} B_r \\ B_\theta \end{bmatrix}.$$

[12] Our primary data set is Magsat measurements re-sampled at 10 s period, and so for a single 30 minute satellite pass between ±50°, we have typically 100–200 data with different values of altitude (r) and geomagnetic colatitude (θ). We thus use an overdetermined linear least squares estimate to evaluate the internal and external coefficients for each satellite pass. We treat dawn and dusk passes separately to accommodate the asymmetry in the ring current structure, which results in different amplitudes for the Dst field in the dusk (ascending) and dawn (descending) passes. Application of least squares estimation to each pass provides an estimate of $i_1^0(t)$ and $e_1^0(t)$ at about 100 minute intervals for 2762 dawn and 2717 dusk orbits. Figures 2a and 2b show exam-
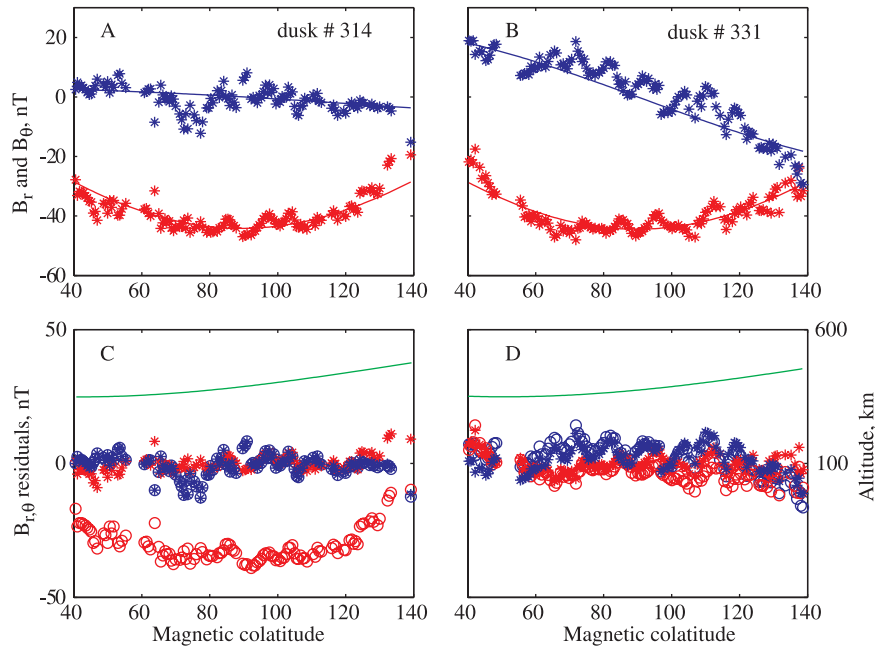
Figure 2. Data, fits, and residuals for two dusk passes. (a, b) Blue represents data (asterisk symbols) and fits (solid lines) to the B_r component and red represents data and fits for the B_θ component. (c, d) Residuals from these fits are again as shown as colored asterisk symbols. Also shown in the bottom panels are the CMP3 residuals (with the Dst correction turned on) for B_r and B_θ as blue and red circles symbols respectively. For pass number 331 (right), the CMP3 model does a good job of fitting the storm-time fields, but for pass 314 (left), CMP3 does poorly, as is evident by the large B_θ residuals. Satellite altitude is shown in green in Figures 2c and 2d.

ples of fits to data from two individual passes of the satellite. The model fits are determined by only two free parameters for each pass, $i_l^m(t)$ and $e_l^m(t)$, with the altitude and magnetic colatitude as fixed data parameters.

[13] It can be seen from Figure 2 that while our fits are quite good, particularly considering that we have only two free parameters, $e_1^0(t)$ and $i_1^0(t)$, for each pass, they are far from perfect. There are many potential sources of error; the existence of non-P_1^0 components of the external field, an imperfectly removed crustal magnetic field, variations in electrical conductivity along the satellite pass, and so on. As one would expect from errors of these types, the residuals have a strong covariance, exhibited as a serial correlation in the misfits, and so one cannot use standard techniques to estimate the linear errors in the estimates of the coefficients. We can, however, compare the residuals after our fitting procedure to those achieved by CMP3 with the Dst correction turned on. We should naturally expect a smaller misfit from our procedure, since it fits the data on a pass by pass basis, while CMP3

uses a global correction for temporal variations in Dst strength via the Dst index. In many case this global correction performs well, see, for example, Figure 2d, but in other cases (Figure 2c) it doesn't do such a good job (demonstrating that we are not simply recovering the Dst index/signal we omitted from the comprehensive model). In this example, there is a large asymmetry in the fitted P_1^0 values between dawn and dusk passes, and while the average of the two agrees fairly well with observatory Dst, the assumption of a symmetric ring current is clearly breaking down.

[14] Table 1 provides a statistical summary of our fitting. Our signal-to-noise ratio is fairly good, particularly for B_θ where it is three or more on average, and much larger during storm times. As expected, our pass by pass fits do a much better job than the comprehensive model with the Dst correction turned on. However, by design, the CMP3 model is constructed based on quiet time variations in the magnetic field (Dst < 20 nT), and Sabaka et al. [2002] report RMS misfits of little more than 4 nT for this data subset.

Table 1. RMS Residuals From all Dusk and Dawn Passes[a]

	Dusk	Dawn
X CMP3-Dst	22.9	15.6
X CMP3	19.2	12.4
B_θ This study	6.0	5.2
Y CMP3	12.0	9.4
Z CMP3-Dst	7.4	6.1
Z CMP3	6.5	5.6
B_r This study	5.2	5.1
N	264391	331977

[a] "This study" represents residuals from fitting our model to the CMP3-Dst data set. For comparison with our CMP3-Dst data set, "CMP3" designates residuals obtained running the comprehensive model with the Dst correction turned on. "N" is simply the number of data supplying the statistics. Note that the results for our study are rotated into geomagnetic coordinates, while the other data are in geographic coordinates.

[15] Plots of $i_1^0(t)$ and $e_1^0(t)$ for dawn and dusk passes are presented in Figure 3. It is immediately apparent that dusk passes are about twice the magnitude of dawn passes, indicating the asymmetry in the ring current morphology. However, the ratio between internal and external fields, about 0.3, is preserved in both time series. This ratio of internal to external fields agrees with value of 0.27 determined by *Langel and Estes*

[1985] and also used by *Olsen et al.* [2000] for the Ørsted initial field model. However, this ratio is frequency-dependent, which we consider below in computing transfer functions between internal and external fields.

5. Replicating Dst

[16] In this section we compare our satellite estimates of the Dst signal strength with those derived from magnetic observatories. Data from low to mid-latitude observatories are used for the Dst index to minimize the influence of both sub-auroral and equatorial electrojets. Hourly H-component magnetic variations are analyzed to remove both the main field baseline and typical quiet-day variations. A cosine factor of the site latitude transforms residual variations to their horizontal field equatorial equivalents. Results from a number of observatories are averaged together. The baseline for Dst is set so that on the internationally designated 5 quietest days the Dst index is zero on average. *Langel et al.* [1980] estimated from Magsat data that the axially symmetric external field was −25 nT when Dst is zero, and this offset is
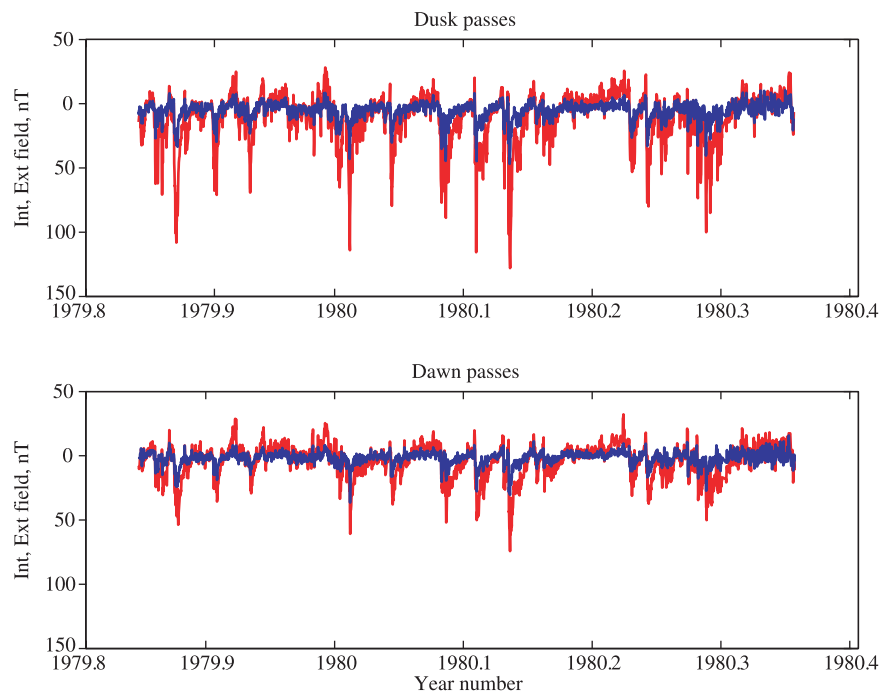

Figure 3. Least squares estimates of $i_1^0(t)$ (blue) and $e_1^0(t)$ (red) from CMP3-Dst residuals. The upper plot is for dusk passes, lower for dawn.
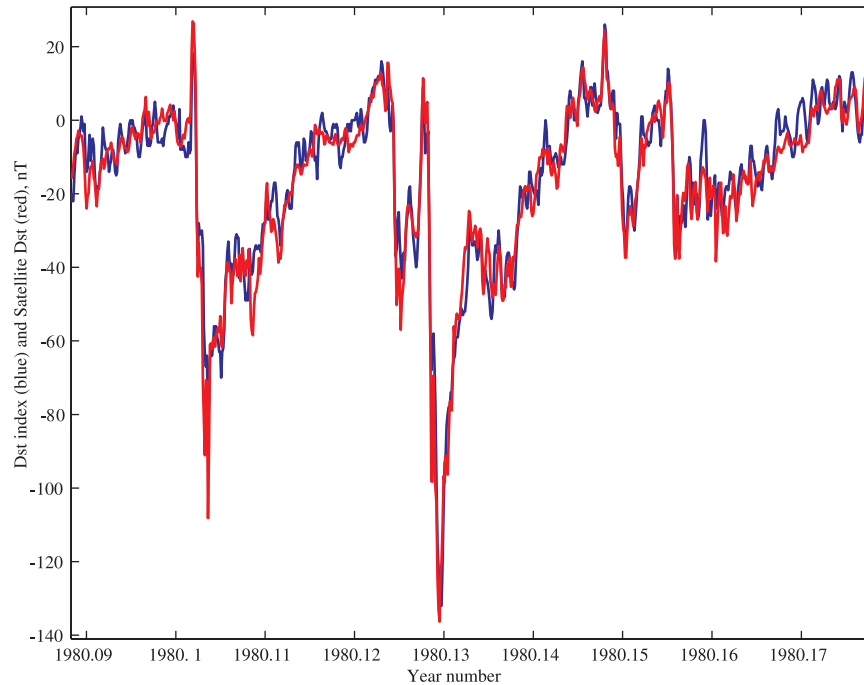
Figure 4. Sum of internal and external field coefficients averaged over dawn and dusk passes ("satellite Dst", red) compared with the Dst magnetic index (blue).

modeled by CMP3. However, the Dst offset may vary with solar cycle.

[17] Our analog of Dst is given by $e_1^0(t) + i_1^0(t)$ averaged over the dawn and dusk passes. This corresponds to a prediction from our fit of the horizontal field intensity at the equator, and may be considered a satellite-derived analog of the Dst index. In order to average the dawn and dusk passes at the same points in time, and to make a comparison with the hourly Dst values, we have interpolated and resampled our $i_1^0(t)$ and $e_1^0(t)$ timeseries using Akima splines [*Akima*, 1970; see also *Lancaster and Salkauskas*, 1986, p. 82]. Our satellite Dst is compared with the actual Dst index from observatory data in Figure 4 for about a month of storm-time data. We see that the satellite analog not only closely follows the structure of Dst, but differs little in amplitude. This validates our estimation procedure for determining the ring current excitation, and suggests an alternative to Dst for characterizing this phenomenon. We quantify the relationship between satellite and observatory Dst estimates in Figure 5. The difference between the two estimates of ring current ampli-

tude has a standard deviation of 5.7 nT. The average difference between $e_1^0(t) + i_1^0(t)$ and Dst is manifest as an offset of 2.4 nT, and not a constant of proportionality. One cannot tell directly which measure is a more faithful estimate of the ring current amplitude, but our fits to the satellite data, exemplified in Figure 2, suggest that the satellite estimates more reliably quantify the local magnitude of the ring current excitation. Both Dst and satellite estimates are temporal averages of the size of the ring current fields; as pointed out by *Olsen* [2002], the satellite estimates do not suffer from a problem in estimating the baseline horizontal magnetic fields. Of course, satellite estimates are only available while satellites fly, and so the traditional Dst index cannot be replaced, merely augmented.

6. 1-D Response Function Estimation

[18] If we only consider conductivity variations as a function of radius within Earth then external field variations $e_1^0(t)$ will induce internal fields $i_1^0(t)$ with P_1^0 structure and a magnitude which depends on
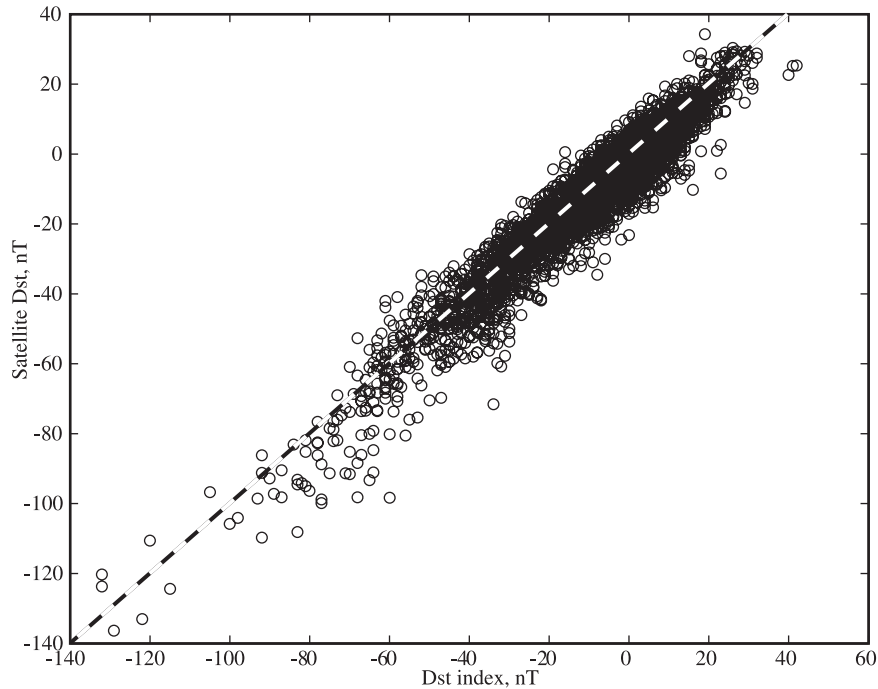
Figure 5. Scatterplot of dawn/dusk average of total field estimated from satellite data ($[e_l^0(t) + i_1^0(t)]/2$) against the Dst index.

Earth conductivity. The frequency dependent transfer function

$$Q_l(f) = \frac{i_l(f)}{e_l(f)}$$

may thus be used to infer conductivity structure within Earth, with higher frequencies corresponding to shallower induced fields. We use multitaper cross-spectral estimation [*Riedel and Sidorenko*, 1995] to evaluate this transfer function, with 20 uniform (as opposed to adaptive) tapers. Figure 6 shows the power spectra of the internal and external fields for the dawn and dusk passes. The dusk passes have greater power than the dawn passes at all frequencies. The lower amplitudes of the dawn passes allow the harmonics of the daily variation, or Sq, to be seen, indicating that the ionospheric contribution has been incompletely removed by the comprehensive model. Figure 7 shows the coherence spectra between $e_1^0(t)$ and $i_1^0(t)$ for the dawn and dusk passes. Overall, the dusk passes have higher coherence than dawn passes. Although there are peaks in the spectra at the harmonics of one day, these correspond to drops in coherence, presumably

because the ionospheric contributions are below the satellite and do not separate coherently into internal and external components.

[19] To evaluate Q_1, we average estimates of the transfer functions using both i_1^0 and e_1^0 as inputs to remove bias associated with noise in the input time series, which in standard spectral analysis is assumed to be noise-free. We carry out band averaging to improve statistical reliability, weighting individual estimates by $\sqrt{1 - \gamma^2}$, where γ is coherency, which is a measure of standard deviation in the estimates. To avoid using daily harmonics and other low-coherence data, we reject data with a coherence-squared less than 0.6. This is a purely heuristic choice based on experimenting with the trade-off between the number of data in the band average versus the uncertainty of the individual estimates used in the average. The dawn coherency spectrum has very few data above this cutoff, and results in estimates of Q_1 that are clearly biased relative to previous estimates, and so we use only the dusk data in our estimates of Q_1.
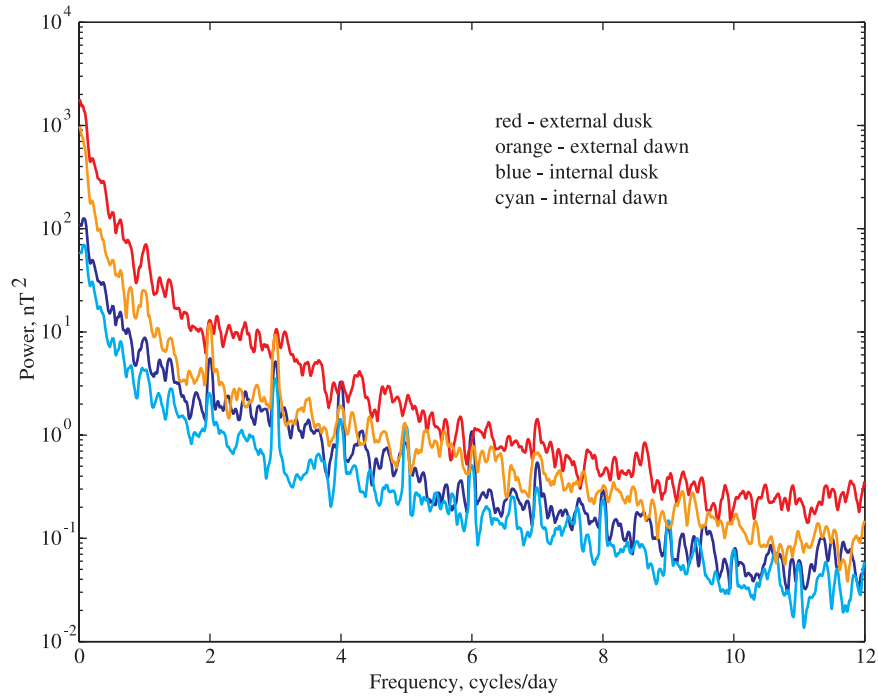
Figure 6. Spectra of the four timeseries shown in Figure 3. It can be seen that the dusk passes have greater power than the dawn passes at all frequencies, and are less contaminated by harmonics of the daily variation.
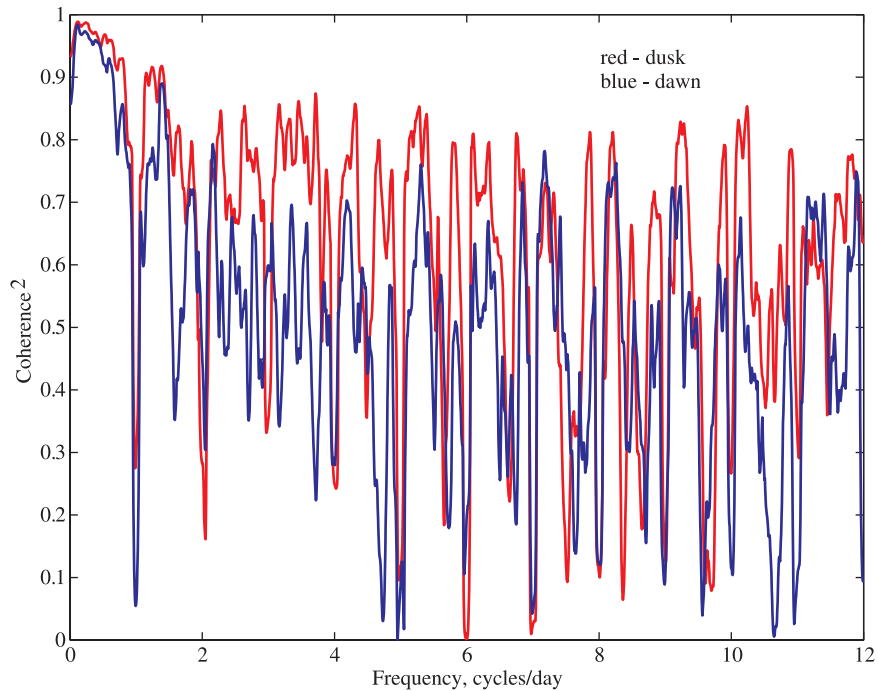

Figure 7. Coherence spectra between $e_1^0(t)$ and $i_1^0(t)$ for the dawn and dusk timeseries. Coherences are higher for the dusk data, but drop at harmonics of one day, presumably because of contamination from ionospheric sources.

Table 2. Satellite Response Functions Derived From the Dusk Passes[a]

Period, s	Re(Q)	Im(Q)	σ Re(Q)	σ Im(Q)	Re(c), km	Im(c), km	σ c, km
21330	0.480	0.0835	0.0021	0.0028	66.9	−363.4	10.5
41410	0.441	0.0788	0.0023	0.0026	240.0	−361.4	11.1
74400	0.383	0.0806	0.0030	0.0034	513.2	−401.1	15.7
185100	0.341	0.0435	0.0017	0.0013	749.4	−230.8	8.2
348000	0.318	0.0358	0.00029	0.00053	872.1	−196.8	2.2
697800	0.313	0.0310	0.0014	0.00058	901.2	−171.9	5.6
1428000	0.282	0.0255	0.0041	0.00048	1079.1	−148.0	13.7
2674000	0.259	0.0216	0.0024	0.0026	1214.3	−130.2	14.9
4593000	0.252	0.00991	0.00099	0.0021	1262.2	−60.4	9.3
11810000	0.249	0.00337	0.000021	0.0010	1278.6	−20.6	3.2

[a] Note that the error estimates σ are from the statistics of the time series analysis, and that an error floor of 50 km in c was used for the inversion studies. Because of the nonlinear relationship between Q and c, independent errors in Real(Q) and Imag(Q) are folded into a single error for the real and imaginary components of c.

[20] Finally, we convert Q_1 to *Weidelt*'s [1972] complex admittance function c using

$$c = a \frac{l - (l+1)Q_l}{l(l+1)(1+Q_l)}$$

where a is the radius of Earth and l is the order of the spherical harmonic function used to estimate Q, in this case 1. Table 2 presents numerical results and Figure 8 shows the resulting satellite response data and *Olsen*'s [1999b] analysis of the same Magsat data set. In the period band from two days to a month, where the two data sets overlap, the agreement is good. Our analysis extends the period range to both shorter and longer periods. Olsen did not attempt to estimate Q at short periods because he used a low-pass filter to remove the effects of ionospheric fields at periods shorter than 30 hours, whereas we address this by coherence weighting. Extension to long periods is possible because the multitaper method allows estimates to be made at periods approaching the length of the data set (in this case 6 months). *Olsen et al.* [2003] recently reported a wider band response function estimated from Ørsted data.

[21] In Figure 9 we compare our Magsat estimates with *Olsen*'s [1999a] compilation of European observatory Dst and Sq data along with an estimate from the 11-year sunspot cycle. Although not shown here, *Constable*'s [1993] compilation of global observatory data agrees well with Olsen's European response. At periods longer than 1 day and shorter than one month, our Magsat estimates are in good agreement with Olsen's data. At shorter periods the satellite data diverges from Olsen's response. This may be explained by the fact that Olsen's response comes from European land-based observatory data, while the satellite response is a global average that includes the oceans. We will support this suggestion in the next section with modeling showing that the short period response is well modeled by a surface conductor.

[22] At long periods (greater than one month), the imaginary component of the satellite response diverges from the European observatory record (and Constable's 1993 compilation), being much smaller in magnitude. We will see from modeling that this corresponds to greater conductivity in the lower mantle than would be interpreted from the observatory data. It is important to ask whether our responses are reliable at these periods, given the short data set we are using. However, we note that both spectral power and coherency are highest at longest periods, and that the real component falls well within the range of the observatory data. Furthermore, the difference between the satellite and observatory responses is significant at a period of one month, where signal power is likely to be strongest. It is unlikely to be a result of a difference between European conductivity structure and global conductivity, since *Constable*'s [1993] compilation follows Olsen's data at these periods. Single observatories can be found that exhibit a similar trend in the imaginary component (the Honolulu response of *Schultz and Larsen* [1987] is shown in Figure 9), but never quite to the same extent.
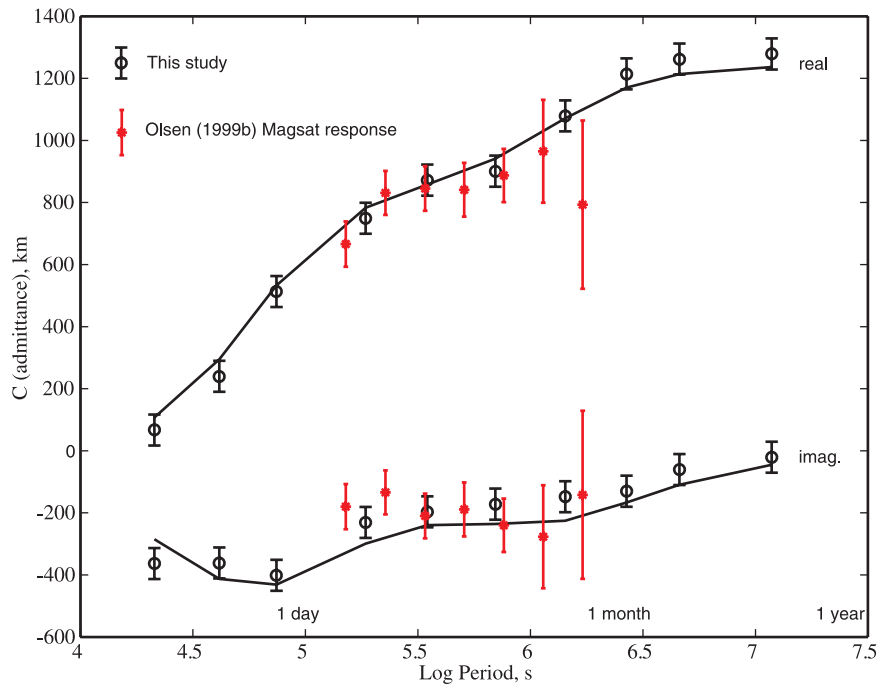
Figure 8. 1-D transfer functions from this study (black), and *Olsen*'s [1999b] study of the same Magsat data set (red). Solid lines show least squares best fitting model responses (D$^+$) for our data.
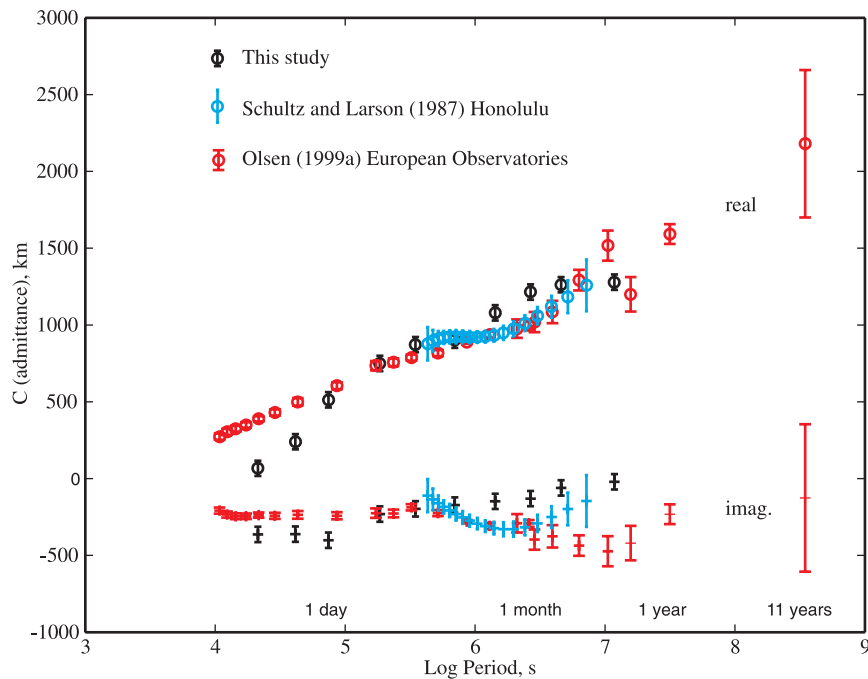

Figure 9. Our Magsat 1-D response function (black), the European observatory average of *Olsen* [1999a] (red) which includes the 11 year estimate of *Harwood and Malin* [1977], and *Schultz and Larsen*'s [1987] response for the Honolulu observatory (blue).

[23] One possible explanation for the long period discrepency lies in the nature of the time series estimation we have used. Each point in our timeseries results from a fit of internal and external P_1^0 components to data which span a range of latitudes and altitudes. Observatory studies either assume a P_1^0 geometry a priori, or, at best, use a range of latitudes to do the fitting. It is therefore possible that the observatory studies are contaminated by non-P_1^0 magnetic fields at the longer periods. We suggest this as a tentative hypothesis, further work will be required to support this idea.

7. 1-D Conductivity Model Estimation

[24] *Parker and Whaler*'s [1981] D^+ algorithm provides the best possible fit to the data in a least squares sense for a 1-D Earth structure. Using error bars estimated from spectral analysis statistics, D^+ fitting provides unacceptable misfits for the response function. Instead, we assign an error floor of 50 km to the data, which corresponds to a D^+ misfit of RMS 0.95. The response of the D^+ model to these modified data is shown by the solid line in Figure 8.

[25] Whilst the D^+ algorithm provides an estimate of the best possible fit to a data set, the model associated with the response function is unphysical, consisting of delta functions of conductivity in an insulating half-space. For more realistic models, we use the Occam algorithm of *Constable et al.* [1987] [see also *Parker*, 1994] which generates a maximally smooth model (measured as the first derivative of log[conductivity] with respect to log[depth]) for a given data misfit. We have modified the implementation of the Occam algorithm in two ways; we have corrected the 1-D forward model calculations for spherical Earth geometry using the method of *Weidelt* [1972], and we have terminated the model with a highly conducting core at a depth of 2886 km.

[26] The one free parameter associated with the Occam approach is the appropriate misfit level. With well behaved error statistics and no features in the data other than those generated by a 1-D model, statistical arguments can be used to choose a misfit level, such as an expected value

of RMS = 1. However, we have already used a more heuristic approach by assigning an error floor based on D^+ fitting. Given this error floor and by examining smooth models at various misfit levels, we present a smooth model fitting the data to RMS 1.15 in Figure 10. The salient features of this model do not change significantly as the misfit is increased or decreased a moderate amount. All models exhibit a large jump from about 0.01 S/m to about 2 S/m at a depth of around 700 km. This feature is seen in many induction studies and is thought to be associated with the phase transition from garnet and olivine spinel above 670 km to magnesiowüstite and silicate perovskite below this depth. There is little evidence for a shallower increase in conductivity at the 440 km phase transition from olivine to beta spinel as predicted by *Xu et al.* [1998]. All models show a further increase in conductivity at a depth of 1300 km. This feature is not widely reported in other studies, and is generated by the small imaginary components of the response function at long period. It is worth noting that this model, while incompatible with *Olsen*'s [1999a] and *Constable*'s [1993] observatory compilations, is in fact compatible with the 11-year response of *Harwood and Malin* [1977].

[27] Both the smooth model and D^+ exhibit a region of increased conductivity near the surface, at depths less than a few tens of kilometers. This feature is not seen when inverting the observatory data, and is a consequence of including the shorter period satellite response collected over both oceans and continents. The D^+ model includes a surface conductance of 8300 S, which is nicely explained by an ocean depth of 2800 km (averaged over seas and continents) and the conductivity of seawater (3 S/m).

[28] The upper mantle conductivity agrees well with a temperature of around 1400°C and the SO2 conductivity-temperature relationship for dry olivine developed by *Constable et al.* [1992]. This is further supported by an estimated 1400°C temperature for the 440 km transition from olivine to spinel [*Katsura et al.*, 1998; *Akaogi et al.*, 1989]. However, the conductance, or conductivity-thickness product, of the average ocean is slightly greater than the conductance of the mantle part of
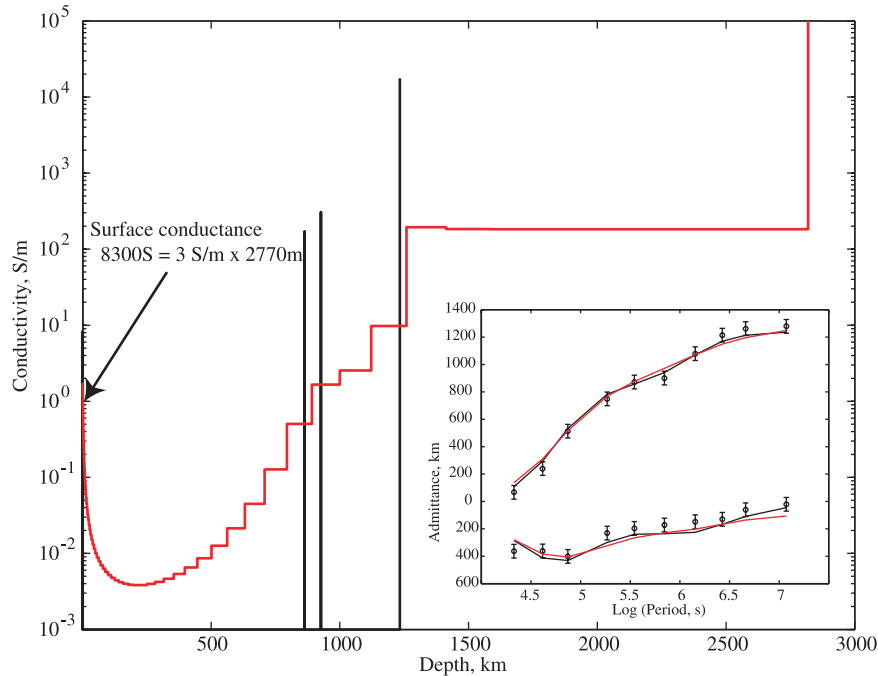
Figure 10. Models generated by Occam smooth inversion (stepped red line) fitting to RMS 1.15 and a graphical representation of the D$^+$ model (vertical bars), which fits the data to RMS 0.95, and plotted assuming a layer thickness of 1/1000 of a decade (i.e., 1 km at a depth of 1000 km) and a conductivity scaled by 1/1000. The D$^+$ model includes a delta function at the surface of conductance 8300 S. The inset shows fits to the data set for both these models.

the section. This implies that resolution in the mantle section, at least beneath the ocean, is poor, and that our ability to discriminate 3-D structure in the mantle will be restricted to regions beneath the continents.

8. A Measure of 3-D Magnetic Induction in Earth

[29] The 1-D inversions demonstrate that the satellite response is sensitive to electrical conductivity as shallow as a few kilometers, and, unlike land-based observatory measurements, contains information about the ocean basins. However, one of the main goals of satellite conductivity studies is the determination of three dimensional (3-D) conductivity structure.

[30] The internal magnetic field $i_1^0(t)$ is induced by the external field $e_1^0(t)$, and so the ratio $i_1^0(t)/e_1^0(t)$ represents some type of global time domain response. By normalizing by the primary field $e_1^0(t)$ we account for variations in magnetospheric activity and also remove dusk/dawn structure in $e_1^0(t)$. We

can study geographic variations in this response by considering its average within $2 \times 3°$ bins. We should, for example, expect to be able to identify the oceanic regions as areas where induction is enhanced by the increased conductivity of seawater, and conversely observe lower induction over continents. Of course, if $i_1^0(t)$ were truly of P_1^0 geometry, it would have no longitudinal variation, but each individual satellite pass will sample a response dominated by the conductivity structure below the satellite. Since dusk and dawn paths cut across lines of longitude in opposite directions, there is some potential to discriminate North-South structure.

[31] Figure 11 provides an image of the induced magnetic field in Earth. We have further normalized the internal fields by $\sqrt{1 + 3\cos^2\theta}$, to remove the dependence on magnetic colatitude θ. We have stacked a total of over 5000 individual satellite passes to get this image. As anticipated, the figure shows systematically lower induced fields over continental areas. Over South America and Africa, both situated near the equator, the lows correspond pleasingly with the actual continent. Asia also has
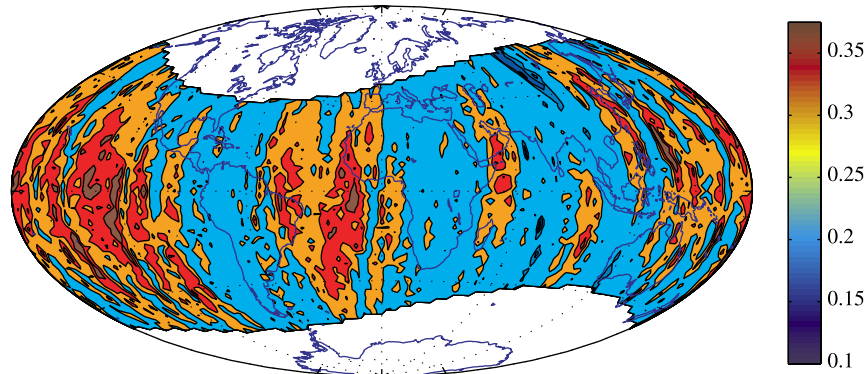
Figure 11. Global induction obtained by combining B_r and B_θ components of normalized induced field, averaged in $2 \times 3°$ bins.

low internal fields, although smearing of the data along the satellite paths has reduced the contrast between Asia and the Indian Ocean.

9. Conclusions

[32] Our analysis of geomagnetic satellite data shows that traditional observatory estimates of Earth electrical impedance can be extended both spatially, by collecting data over oceans, and in frequency, by collecting shorter period data that are sensitive to crustal conductivities. Excellent agreement between our estimates of P_1^0 ring current intensity and the Dst index strongly suggests that our analysis technique is valid. Indeed, for some purposes our estimates of satellite Dst are probably more accurate than the traditional index, although the satellite measurements are limited in spatial extent during any one pass, and the temporal extent of the record is limited by the misson length.

[33] Inversion for radial conductivity structure demonstrates that our satellite responses are sensitive to conductivities as shallow as the oceans, and indeed we recover the average conductivity-thickness product of the global ocean very well. The upper mantle appears in our models as relatively uniform in conductivity at 0.01 S/m, corresponding to a dry olivine mantle of about 1400°C, although this should probably be considered an upper bound for conductivity since resistors sandwiched between conductors (in this case the oceans and lower mantle) are poorly resolved by geomagnetic

methods. We see little evidence for a large increase in conductivity in the transition zone, but in addition to an increase in conductivity at the top of the lower mantle we see a further increase at a depth of about 1300 km.

[34] By relying on redundant data and stacking statistics, we are able to get a 3-D image of induced fields, which shows increased induction over the conductive oceans and smaller induced fields beneath the continents. More, and better quality, data from Ørsted, Champ, and future satellite missions will improve these responses significantly. Finally while traditional conductivity estimation from induced fields is carried out in the frequency domain, as was done here, the 3-D problem may best be tackled in the time domain, using an extension of the two-dimensional approach described by *Martinec and Everett* [2003] and the 3-D forward modeling of *Velímský et al.* [2003].

10. Appendix

[35] Data sets used and generated by this work may be downloaded from http://mahi.ucsd.edu/Steve/MDAT/.

Acknowledgments

References

Akaogi, M., E. Ito, and A. Navrotsky (1989), Olivine-modified spinel-spinel transitions in Mg2SiO4-Fe2SiO4: Calorimetric measurements, thermochemical calculations, and geophysical application, *J. Geophys. Res.*, *94*, 15,671–15,685.

Akima, H. (1970), A new method of interpolation and smooth curve fitting based on local procedures, *J. Assoc. Comput. Mach.*, *17*, 589–602.

Banks, R. J. (1969), Geomagnetic variations and the conductivity of the upper mantle, *Geophys. J. R. Astron. Soc.*, *17*, 457–487.

Chapman, S., and J. Bartels (1940), *Geomagnetism*, vol 1, 542 pp., Clarendon, Oxford, England.

Constable, S. (1993), Constraints on mantle electrical conductivity from field and laboratory measurements, *J. Geomag. Geoelect.*, *45*, 707–728.

Constable, S. C., R. L. Parker, and C. G. Constable (1987), Occam's Inversion: A practical algorithm for generating smooth models from EM sounding data, *Geophysics*, *52*, 289–300.

Constable, S., T. J. Shankland, and A. Duba (1992), The electrical conductivity of an isotropic olivine mantle, *J. Geophys. Res.*, *97*, 3397–3404.

Daglis, I. A., R. M. Thorne, W. Baumjohann, and S. Orsini (1999), The terrestrial ring current: Origin, formation, and decay, *Rev. Geophys.*, *37*, 407–438.

Didwall, E. M. (1984), The electrical conductivity of the upper mantle as estimated from satellite magnetic field data, *J. Geophys. Res.*, *89*, 537–542.

Harwood, J. M., and S. R. C. Malin (1977), Sunspot cycle influence on the geomagnetic field, *Geophys. J. R. Astron. Soc.*, *50*, 605–619.

Katsura, T., K. Sato, and E. Ito (1998), Electrical conductivity of silicate perovskite at lower mantle conditions, *Nature*, *395*, 493–495.

Lahiri, B. N., and A. T. Price (1939), Electromagnetic induction in non-uniform conductors, and the determination of the conductivity of the earth from terrestrial magnetic variations, *Philos. Trans. R. Soc. A*, *237*, 64.

Lancaster, P., and K. Salkauskas (1986), *Curve and Surface Fitting*, Academic, San Diego, Calif.

Langel, R. A., and R. H. Estes (1985), Large-scale, near-field magnetic fields from external sources and the corresponding induced internal field, *J. Geophys. Res.*, *90*, 2487–2494.

Langel, R. A., and W. J. Hinze (1998), *The Magnetic Field of the Earth's Lithosphere: The Satellite Perspective*, 429 pp., Cambridge Univ. Press, New York.

Langel, R. A., R. H. Estes, G. D. Mead, E. B. Fabiano, and E. R. Lancaster (1980), Initial geomagnetic field model from Magsat vector data, *Geophys. Res. Lett.*, *7*, 793–796.

Martinec, Z., and M. E. Everett (2003), Two-dimensional spatio-temporal modelling of satellite electromagnetic induction signals, in *First CHAMP Mission Results for Gravity, Magnetic and Atmospheric Studies*, edited by C. Reigber, H. Lühr, and P. Schwinzer, pp. 27–321, Springer-Verlag, New York.

Olsen, N. (1999a), Long-period (30 days-1 year) electromagnetic sounding and the electrical conductivity of the lower mantle beneath Europe, *Geophys. J. Int.*, *138*, 179–187.

Olsen, N. (1999b), Induction studies with satellite data, *Surv. Geophys.*, *20*, 309–340.

Olsen, N. (2002), A model of the geomagnetic field and its secular variation for epoch 2000 estimated from Ørsted data, *Geophys. J. Int.*, *149*, 454–462.

Olsen, N., et al. (2000), Oersted initial field model, *Geophys. Res. Lett.*, *27*, 3607–3610.

Olsen, N., S. Vennerstrøm, and E. Friis-Christensen (2003), Monitoring magnetospheric contributions using ground-based and satellite magnetic data, in *First CHAMP Mission Results for Gravity, Magnetic and Atmospheric Studies*, edited by C. Reigber, H. Lühr, and P. Schwinzer, pp. 245–250, Springer-Verlag, New York.

Oraevsky, V. N., N. M Rotanova, V. Y. Semenov, T. N. Bondar, and D. Y. Abramova (1993), Magnetovariational sounding of the Earth using observatory and Magsat satellite data, *Phys. Earth. Planet. Inter.*, *78*, 119–130.

Parker, R. L. (1994), *Geophysical Inverse Theory*, Princeton Univ. Press, 386 pp., Princeton, N. J.

Parker, R. L., and K. A. W. Whaler (1981), Numerical methods for establishing solutions to the inverse problem of electromagnetic induction, *J. Geophys. Res.*, *86*, 9574–9584.

Riedel, K., and A. Sidorenko (1995), Minimum bias multiple taper spectral estimation, *IEEE Trans. Signal Process.*, *43*, 188–195.

Sabaka, T., N. Olsen, and R. A. Langel (2000), A comprehensive model of the near-Earth magnetic field: Phase 3, *NASA TM-2000-209894*, 75 pp.

Sabaka, T., N. Olsen, and R. A. Langel (2002), A comprehensive model of the near-Earth magnetic field: Phase 3, *Geophys. J. Int.*, *151*, 32–68.

Schultz, A., and J. C. Larsen (1987), On the electrical conductivity of the mid-mantle: 1. Calculation of equivalent scalar magnetotelluric response functions, *Geophys. J. R. Astron. Soc.*, *88*, 733–761.

Schultz, A., and J. C. Larsen (1990), On the electrical conductivity of the mid-mantle: 2. Delineation of heterogeneity by application of extremal inverse solutions, *Geophys. J. R. Astron. Soc.*, *101*, 565–580.

Schuster, A. (1889), The diurnal variation of terrestrial magnetism, *Philos. Trans. R. Soc. A*, *180*, 467–518.

Sugiura, M. (1964), Hourly values of equatorial Dst for the IGY, *Ann. Int. Geophys. Year*, *35*, 9–45.

Velímský, J., M. E. Everett, and Z. Martinec (2003), The transient Dst electromagnetic induction signal at satellite altitudes for a realistic 3-D electrical conductivity in the crust and mantle, *Geophys. Res. Lett.*, *30*(7), 1355, doi:10.1029/2002GL016671.

Weidelt, P. (1972), The inverse problem of geomagnetic induction, *Zeit. Geophys.*, *38*, 257–289.

Xu, Y., B. T. Poe, T. J. Shankland, and D. C. Rubie (1998), Electrical conductivity of olivine, wadsleyite, and ringwoodite under upper-mantle conditions, *Science*, *280*, 1415–1418.